Journal of Marine Science and Application (2026) 25: 1225-1237
https://doi.org/10.1007/s11804-025-00757-7

RESEARCH ARTICLE

Analytical Study on a Quasi-Zero-Stiffness Vibration Isolator Based on Magnetic Rings and Disc Springs

Mengtong Wang[1], Chang Qi[2], Sheng Li[1], Rui Li[2], Liqiang Han[2] and Hao Chen[2]

Received: 01 April 2025 / Accepted: 17 July 2025
© Harbin Engineering University and Springer-Verlag GmbH Germany, part of Springer Nature 2026

Abstract

A suitable quasi-zero-stiffness (QZS) vibration isolator system was developed for confined installation spaces. The system achieves close-to-zero stiffness through the parallel combination of magnetic rings and disc springs. First, the Halbach magnetization method was proposed for the positive stiffness mechanism owing to its advantages in the field of non-contact transmission. Furthermore, the negative stiffness mechanism was designed based on the nonlinear stiffness characteristics of disc springs. Next, the proposed QZS vibrator isolator was structurally optimized by focusing on the interaction between the positive and negative stiffness mechanisms. Thereafter, the effects of key structural and operating parameters on its dynamic characteristics (e. g., resonance frequency and force transmissibility (T_e)) were analyzed to validate the accuracy of the theoretical model. Finally, comparative experiments were conducted using a magnetic bearing testing platform to evaluate T_e through the QZS vibration isolator and its equivalent linear isolator under identical excitation. The results demonstrated that the QZS vibration isolator exhibited superior low-frequency vibration isolation performance. This study offered a basis for prototype manufacturing, future experimental validations, and broadening engineering implementation.

Keywords Halbach; Quasi-zero-stiffness vibration isolator; Nonlinear dynamics; Low-frequency vibration control; Adjustable operating condition

1 Introduction

The inevitable vibration generated during vessel operation creates underwater radiated noise, which critically increases the susceptibility of the vessel to sonar detection and necessitates enhanced acoustic stealth performance to improve tactical advantage (operational effectiveness and survivability). However, conventional linear vibration isolators are inherently limited by their structural characteristics; they achieve effective vibration isolation only when the excitation frequency exceeds a certain multiple of the natural frequency of the system (Dong et al., 2018). A conventional design strategy for linear isolation systems involves lowering the natural frequency to enhance isolation efficiency. Nevertheless, this approach inevitably compromises the load-bearing capacity of the system, thereby creating a trade-off in the design of these isolators (Dalela et al., 2022).

To resolve the inherent drawbacks of linear vibration isolators, design methods have been proposed based on structures exhibiting superior negative stiffness properties. Among these designs, spring types (Liu et al., 2021; Tian et al., 2023; Zhou et al., 2015), Euler-beam types (Cai et al., 2020; Davis and McDowell, 2017; Liu et al., 2021), and magnetic spring types (Chai et al., 2017; Wang et al., 2022; Yan et al., 2018; Zhang et al., 2023) have been extensively investigated. Notably, these designs also exhibited inherent structural limitations, including instability, large installation space requirements, and poor partial loading resistance. (Ma et al., 2023) reported a novel disc-spring isolation system that mitigates Coulomb friction by incorporating loading rings, thereby enhancing the seismic-isolation capabilities. The effectiveness of the loading rings was validated by theoretical analyses and cyclic loading tests. However, the researchers failed to account for the long-term

Article Highlights

- Novel Parallel Design Combining a Halbach Magnet Array with Disc Springs.
- Systematic Structural Parameter Optimization for Ultra-Low Natural Frequency.
- Integrated Theoretical-Simulation-Experimental Validation Demonstrating Superior Low-Frequency Performance.

✉ Sheng Li
shengli@dlut.edu.cn

[1] School of Naval Architecture, Dalian University of Technology, Dalian 116024, China

[2] School of Automotive Engineering, Dalian University of Technology, Dalian 116024, China

durability of the loading rings under varying environmental conditions. (Liu et al., 2024) analyzed a disc-spring-based stiffness device, termed the negative–positive–uncoupled stiffness device (NPUSD), which enhances multi-level seismic fortification. The incorporation of combined disc springs allowed for the independent adjustments of stiffness ranges, thereby effectively improving seismic mitigation. However, they did not comprehensively explore the long-term durability and maintenance requirements of NPUSD in practical scenarios. (Hao et al., 2022) analyzed a flexible-plate-supported nonlinear vibration isolator using a combination of Lagrange's method, an improved Fourier series, and the Rayleigh–Ritz method to derive modal coefficients. The experimental validation confirmed that adjusting the stiffness and damping parameters improved isolation performance. (Zhang et al., 2025) investigated an inclined beam isolator based on thermoplastic polyurethane. This isolator integrates quasi-zero stiffness (QZS) and fractional derivative (FD) damping (QZS−FD). They also developed a dynamic model, which was validated by experimental results. Thus, they demonstrated the superior performance of the isolator and verified the accuracy of the demonstrated QZS–FD model. (Lu et al., 2024) explored the free-vibration characteristics of a vertical QZS isolation system, specifically exploring the loading position of the disc spring. By integrating a negative-stiffness disc spring with a positive-stiffness spiral spring, they realized QZS properties, which were analyzed using the Jacobi elliptic functions and the Newton−harmonic balance approach. However, the omission of damping effects might limit the practical applicability of their findings. Despite this, their study identified and investigated the influences of key factors, including damping characteristics, stiffness ratio, and inclination angle, and investigated their influence on the overall vibration isolation effectiveness.

To address the inherent limitations of linear vibration isolators, namely their inability to simultaneously deliver satisfactory low-frequency isolation performance and realize sufficient load-bearing capacity, studies proposed the combination of structures featuring Halbach magnetic arrays and negative-stiffness disc springs. Based on the variable-stiffness characteristics of disc springs as well as their advantages in compact installation spaces, integrating these elements would effectively overcome the inherent shortcomings of conventional linear vibration isolation systems. First, the relationships between the air gap length and magnetic flux density with the magnetic force were compared across four magnetization methods, demonstrating that Halbach's magnetization induced a stronger magnetic field in the air gap.

Next, the positive-stiffness mechanism was designed, establishing a configuration of four magnetic rings and five aluminum rings. The influence of the height of the aluminum ring on the magnetic field performance was analyzed. Thereafter, the effects of the high-thickness ratio and inner-to-outer diameter ratio on the performance of the disc springs were investigated, after which the structural configuration of the QZS isolator was proposed. This isolator realized a natural frequency of 0.83 Hz, enriching the technical methods for low-frequency vibration isolation. Subsequently, the recovery force and stiffness models of the QZS isolator were established, the negative-stiffness working range was identified, the dynamic model of the system was developed, and the influences of the excitation amplitude (F_0) and damping ratio (c) on the force transmissibility (T_e) of the isolator were analyzed. Finally, the isolation performance of the QZS vibration isolator was validated under harmonic excitation and random vibration.

2 Structural design and analysis of static characteristics

2.1 Magnetic field analysis

The various typical permanent magnet magnetization configurations are illustrated in Figure 1, with the arrows indicating magnetization orientations. Specifically, Configuration (A1) represented axial alternating magnetization, which facilitated the manufacturing process by ensuring magnetic pole uniformity. Configuration (A2) illustrated radial alternating magnetization, which yielded a more uniform magnetic field distribution within the surrounding space. Configuration (A3) depicted a counterclockwise Halbach magnetization arrangement, whereas configuration (A4) exhibited a Halbach magnetization structure integrating radial polarization and axial magnetization, featuring an inner counterclockwise and outer clockwise arrangement. Different combinations of magnetization configurations caused variations in the magnetic flux density and utilization efficiency within the air gap, which consequently generated varying intensities of magnetic forces.

The size of the air gap between the magnets significantly influenced the magnetic flux density. Assuming air gap lengths of 10, 18, and 25 mm, the relationship between magnetic force and displacement was compared across various magnetization configurations. Figure 2 shows that the maximum magnetic forces of A1 were 4416, 1701, and 770 N for air gap lengths of 10, 18, and 25 mm, respectively. For A2, the corresponding maximum magnetic forces were 4304, 1656, and 751 N, and for A3, they were 1305, 471, and 309 N. For A4, the maximum forces reached 5633, 3269, and 2083 N under identical conditions. These results indicated that increasing the air gap length using the same permanent magnet quantity and grade reduced the magnetic flux density and, consequently, decreased the magnetic force.

The magnetic flux density in the air gap, which is defined

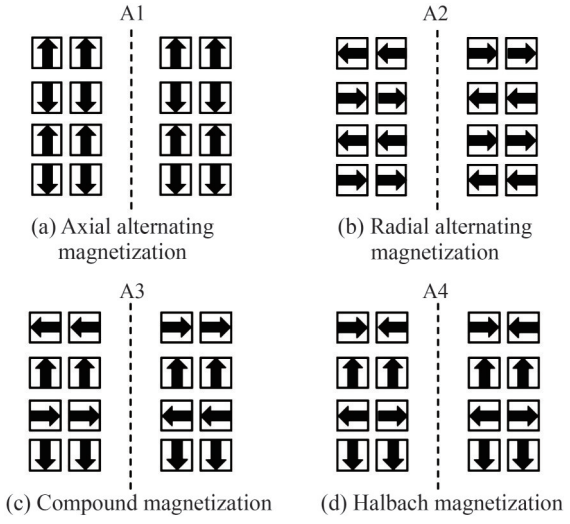


Figure 1 Schematic of the four magnetization configurations

as the magnetic field intensity between the rotor and stator, represents the output capability of the magnetic array and the uniformity and symmetry of the magnetic field distribution. As shown in Figure 3, increasing the air gap lowered the maximum magnetic flux density, thereby decreasing the output force of the magnet array while improving the magnetic field uniformity.

A magnetic-ring positive stiffness mechanism was designed based on the research findings (the preliminary comparative analysis of permanent magnet configurations (A1, A2, A3, and A4) and the influence of the air gap size on the magnetic force). A cross-sectional schematic is presented in Figure 4. This mechanism consisted of stator magnetic rings (1), aluminum rings (2), rotor magnetic rings (3), and a magnet-array housing (4). Each magnet array comprised four layers of magnetic rings alternating with five layers of aluminum rings. The stator and rotor magnetic rings were installed coaxially, with aluminum rings sandwiched between each corresponding stator–rotor layer. The magnet-array housing, which was constructed from stainless steel, was exclusively installed on the outer and inner circumferences of the stator and rotor magnet arrays, respectively, to provide structural support. The magnetic-ring positive stiffness mechanism was primarily designed to deliver static load-bearing capacity and counteract the negative stiffness introduced by disc springs, thereby effectively reducing the natural frequency of the system. The simplified two-dimensional model (Figure 5) was established to streamline theoretical analyses and numerical simulations.

To install the magnets, aluminum rings were sandwiched between each magnetic layer. Therefore, analyzing the impact of these aluminum rings on the performance of the magnetic circuit was critical. Here, the relationship between magnetic force and displacement was investigated at different aluminum ring heights, which were set to 2, 4, and 6 mm. As illustrated in Figure 6, an increase in the aluminum ring height caused a decrease in the maximum magnetic force output and a corresponding increase in the axial displacement at which this maximum force was exerted. This was primarily due to the eddy current effect induced by electromagnetic induction, which generated a counter-

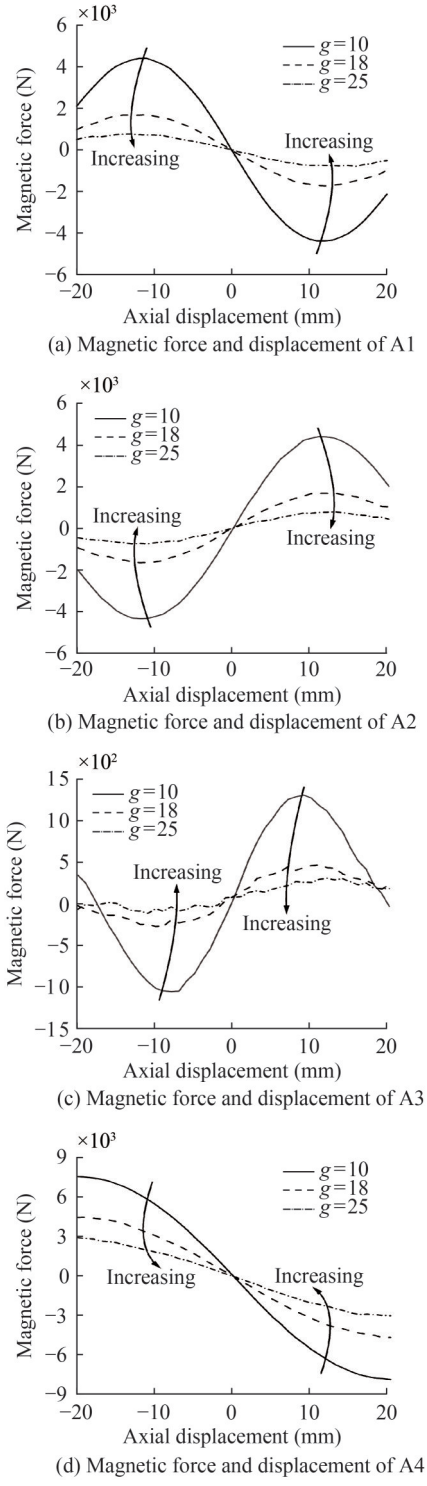
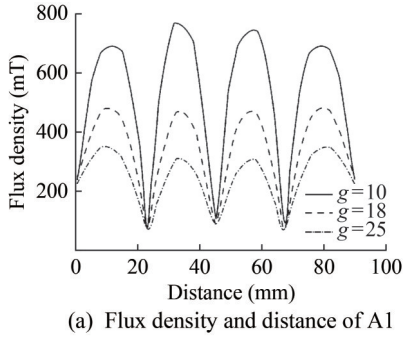
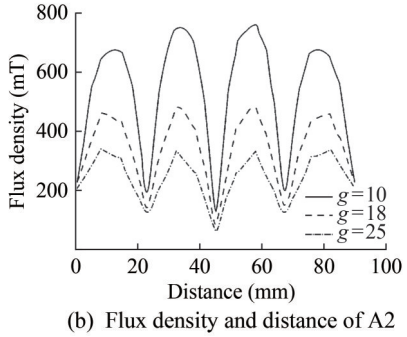


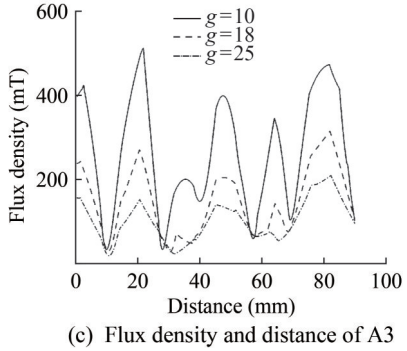
Figure 2 Chart of magnetic force versus air gap length



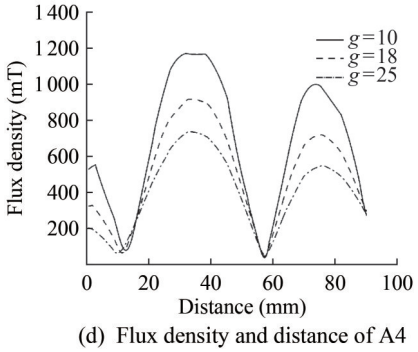
(a) Flux density and distance of A1



(b) Flux density and distance of A2



(c) Flux density and distance of A3



(d) Flux density and distance of A4

Figure 3 Chart of the magnetic flux density versus the air gap length

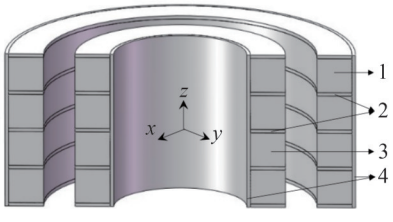


Figure 4 Cross-sectional schematic of the positive-stiffness mechanism

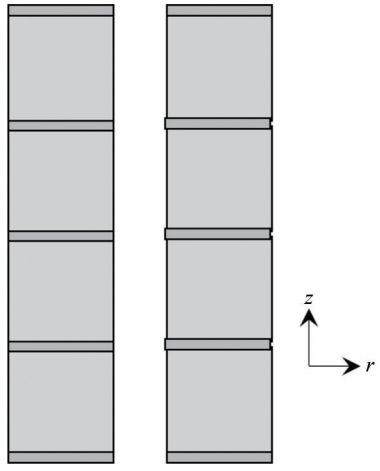


Figure 5 Simplified two-dimensional model of the magnetic ring

acting magnetic field within the aluminum ring, thereby weakening a portion of the original magnetic field. The axial position corresponding to the maximum magnetic force was related to the heights of the aluminum ring and magnet, as shown by the expression:

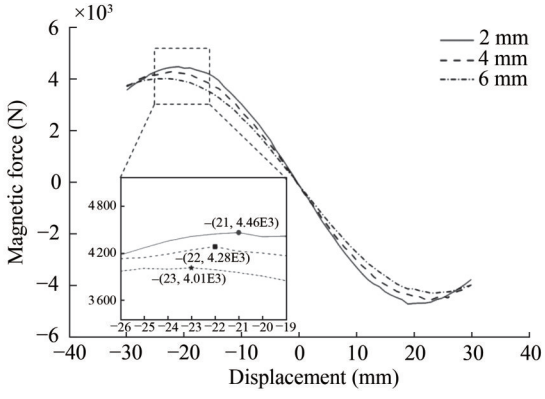


Figure 6 Chart of the effect of the aluminum ring height on magnetic force

$$x_{\max} = h_m + \frac{h_a}{2} \tag{1}$$

where $x_{\max}$ is the displacement corresponding to the maximum magnetic force and h_m and h_a are the heights of the magnet and aluminum rings, respectively.

After comparing the magnetic force and magnetic flux density across different magnetization methods, the A4 magnetization configuration was ultimately selected as the optimum. This approach simultaneously enhances the magnetic field on the air gap side and weakens it in the opposite direction, thereby achieving the maximum magnetic flux density and magnetic force with a minimal amount of magnetic material. Figures 7, 8 illustrate the mathematical model for two parallel rectangular-section permanent magnets. In this model, F_{zij} and F_{xij} are defined as the magnetic forces exerted by the jth inner magnetic ring on the ith

outer magnetic ring in the z (axial) and x (radial) directions of the bearing, respectively. The axial distances between the jth and ith inner and outer magnetic rings, respectively, are represented by $c_{ij} = c + (j - i)a, \beta_i = \theta_0 + (i - 1)\theta$, and $\beta_j = \theta_0 - (j - 1)\theta$, where θ_0 denotes the initial angle between the magnetic ring orientation and the positive x-axis and θ is the incremental angle per step. Based on the virtual work principle in the electromagnetic field theory (Tian et al., 2017), the magnetic force per unit length between two infinitely long, thin-strip permanent magnets can be derived as follows:

$$dF_z = \frac{B_{r1}B_{r2}}{\pi\mu_0 r_1^3}\sin(\beta_1 + \beta_2 - 3\theta)ds_1 ds_2 \tag{2}$$

$$dF_x = -\frac{B_{r1}B_{r2}}{\pi\mu_0 r_1^3}\cos(\beta_1 + \beta_2 - 3\theta)ds_1 ds_2 \tag{3}$$

where r_1 is the distance from points M to P; B_{r1} and B_{r2} denote the residual magnetic induction intensities of the permanent magnets, β_1 and β_2 are the angles between j_1 and j_2 and the positive direction of the x-axis, respectively; θ is the angle between r_1 and the positive x-axis direction; and μ_0 is the permeability of free space, with a value of $4\pi \times 10^{-7}$ H/m.

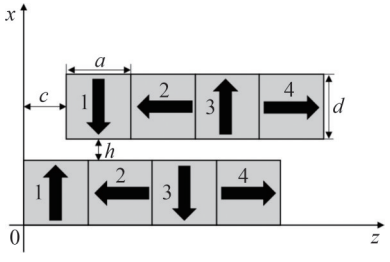


Figure 7 Schematic of the Halbach magnetization configuration

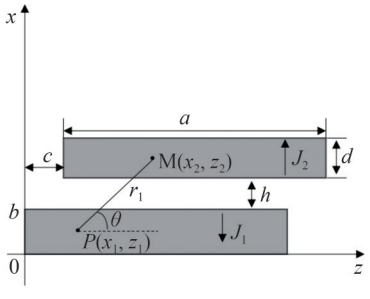


Figure 8 Mathematical model of two parallel rectangular sections

Equations (2) and (3) only apply to the calculation of the magnetic force between two parallel magnets at a specific displacement. When axial movement occurs between the inner and outer magnetic rings, parameters, such as the angle between the magnets and the center-to-center distance, change dynamically. Owing to the complexity of these variations, theoretically analyzing the motion state and resulting magnetic force is highly challenging. Rather, a specific analysis must be performed based on the given boundary and initial conditions. For instance, finite element analysis, as one of the most effective and widely employed numerical computation methods, provides a practical approach to addressing these challenges.

To guide the structural design and develop an optimized QZS vibration isolator, Maxwell software was employed to model and simulate the structure displayed in Figure 4, based on the structural dimensions listed in Table 1. Figure 9 shows the magnetic flux density distribution of the positive-stiffness mechanism of the magnetic rings. The figure confirmed that the Halbach magnetization method enhanced the magnetic field on one side of the magnetic poles, facilitating the generation of a stronger magnetic force.

Table 1 Parameters of the magnetic ring mechanism

Name	Value (mm)	Name	Value (mm)
Rotor inner diameter	40	Rotor outer diameter	60
Stator inner diameter	78	Stator outer diameter	98
Air gap length	18	Magnetic ring height	20
Aluminum ring height	2	Number of magnetic layers	4

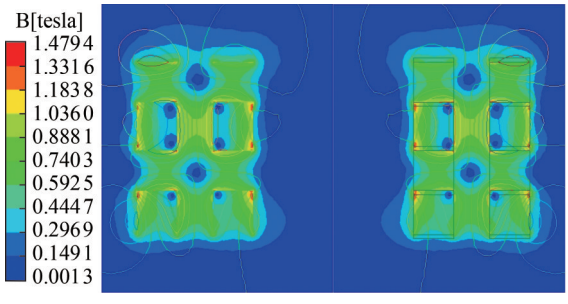


Figure 9 Chart of the magnetic flux density under Halbach magnetization

In this study, the "inner reverse, outer forward" Halbach magnetization method was adopted. Additionally, the magnetic force and midline magnetic flux density within the air gap were compared for this method and three other magnetization methods when the air gap length was set to 18 mm. Under an equivalent amount of magnetic material and the same air gap length, the magnetic-circuit design based on the Halbach magnetization method demonstrated advantages in enhancing the magnetic energy product and improving magnet-utilization efficiency, ultimately resulting in superior magnetic performance (Figures 10 and 11).

Next, the air gap length was fixed at 18 mm. Figure 12 shows the variation of magnetic force with displacement for the Halbach magnetization method in the positive-stiffness mechanism. Considering the limitations of the theoretical expression, subsequent magnetic force calculations were performed using a simulation-based fitting expression.

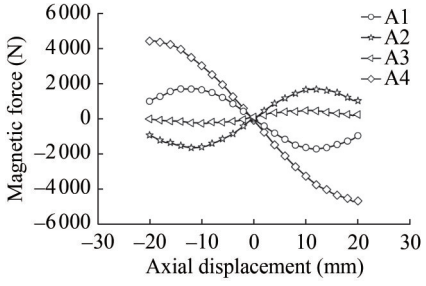


Figure 10 Comparison of the magnetic force generated using four magnetizing methods

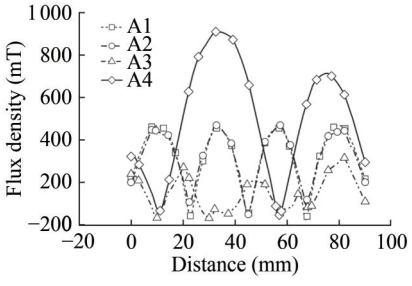


Figure 11 Comparison of magnetic flux densities obtained by the four magnetizing methods

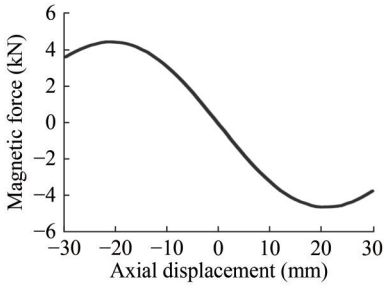


Figure 12 Chart of magnetic force versus displacement for the Halbach magnetization method

By fitting the curve in Figure 12, the simulation-based fitting expression for the magnetic force in the x-direction under the Halbach magnetization condition was obtained, as detailed in Equation (4).

$$F_c = 2.362 \times 10^{-4} x^3 - 2.054 \times 10^{-5} x^2 + 0.326\,9x + 0.115\,9 \tag{4}$$

where x is the displacement of the axial motion of the magnet.

2.2 Static characterization of negative-stiffness mechanisms

The disc spring (Ozaki et al., 2012) was a conical compression spring, which was formed by stamping a steel plate. It exhibited high stiffness and could withstand large loads with minimal deformation, making it suitable for applications with limited axial installation space and high load-bearing requirements.

Further, the disc spring was primarily classified into two types: those with and without support surfaces. It was assumed that the external load and reaction force on the support surface were distributed along the inner and outer circumferences. As it was also assumed that the material was perfectly elastic, the frictional effects on the contact surface were neglected. Notably, the relationship between the load, stiffness, and displacement deformation for the disc springs without support surfaces was determined by Equations (5) and (6):

$$F = \left(\frac{4E}{1-\mu^2}\right)\left(\frac{t^4}{K_1 D^2}\right)\left(\frac{x}{t}\right)\left[\left(\frac{h_0}{t}-\frac{x}{t}\right)\left(\frac{h_0}{t}-\frac{x}{2t}\right)+1\right] \tag{5}$$

$$K = \left(\frac{4E}{1-\mu^2}\right)\left(\frac{t^3}{K_1 D^2}\right)\left[\left(\left(\frac{h_0}{t}\right)^2 - 3\left(\frac{h_0}{t}\right)\left(\frac{x}{t}\right)+\frac{3}{2}\left(\frac{x}{t}\right)^2\right)+1\right] \tag{6}$$

where $K_1 = \frac{1}{\pi}\cdot\frac{\left(\frac{C-1}{C}\right)^2}{\left(\frac{C+1}{C}\right)-\frac{2}{\ln C}}$, $C = \frac{D}{d}$.

where F represents dead loads; E is the modulus of elasticity of the structural material; D and d are the outer and inner diameters of the disc spring, respectively; μ is Poisson's ratio; h_0 is the height of the disc spring; t is its thickness; and x is displacement.

The effects of the height–thickness (h_0/t) and inner–outer diameter (D/d) ratios on the performance of the disc springs were also analyzed. As shown in Figure 13, at $h_0/t < 1.5$, the load-bearing capacity of the springs increased with displacement. At $h_0/t = 1.5$, the load-bearing capacity remained nearly constant with the displacement, indicating the close-to-zero stiffness. At $h_0/t > 1.5$, a negative-stiffness region appeared, although the load-bearing capacity decreased significantly.

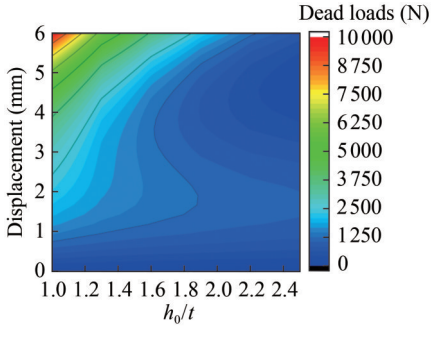


Figure 13 Effect of h_0/t on the load-bearing capacity

As shown in Figure 14, a smaller D/d resulted in a higher load-bearing capacity. However, owing to installation and design constraints, this ratio is typically set between 1.7 and 2.5 for engineering applications.

Based on the explored influence of the structural parameters of the disc springs on their performance, a negative-stiffness mechanism was designed using a disc spring with-

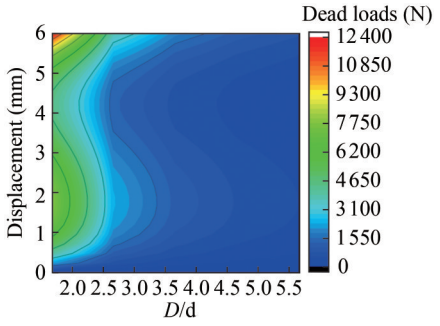


Figure 14 Effect of *D/d* on the load-bearing capacity

out a support surface. The structural parameters of this mechanism are presented in Table 2.

Table 2 Structural parameters of the disc spring without a support surface

Name	Value (mm)	Name	Value (mm)
Disc spring outer diameter (*D*)	130	Disc spring inner diameter (*d*)	40
Disc spring thickness (*t*)	1.5	Disc spring height (*h*)	4.9

2.3 Structural design

A dual-mechanism magnetic-ring QZS vibration isolator is presented in this study (Figure 15). It comprises the magnetic positive-stiffness mechanism and the disc springs negative-stiffness mechanism. Further, the negative-stiffness mechanism consisted of six layers of composite disc springs arranged in two opposing pairs and two stacked groups. Additionally, these disc springs were nested onto a disc spring base, which supported them and restricted displacement. Conversely, the positive-stiffness mechanism comprised four layers of internal and external magnetic rings, five layers of internal and external aluminum rings, and support rods sandwiched between the rings. The primary function of this positive-stiffness mechanism was to counterbalance the negative stiffness and impart the isolation system with a static load-bearing capacity. Its magnetic and aluminum rings were installed alternately along the support rods, and its central shaft was securely connected to the inner housing, which, together with the aluminum rings, fixed the magnetic rings and prevented structural instability due to excessive magnetic forces. Further, the disc spring base was bolted to the base to avoid instability due to uneven loading. The upper end cover reduced magnetic flux leakage, thereby enhancing magnetic performance. When the isolated object was placed on the loading platform, equilibrium was achieved when the gravitational force of the object was balanced by the combined preload, magnetic force, and disc spring force.

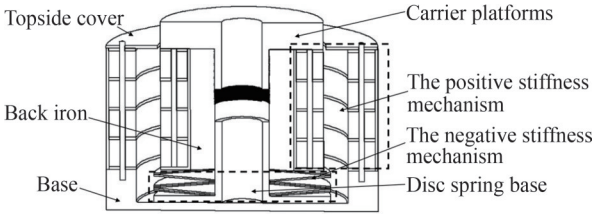


Figure 15 Cross-sectional schematic of the QZS isolator

3 Dynamic characterizations

3.1 Calculations of the return force and stiffness

The proposed magnetic-ring QZS vibration isolator was obtained by integrating the magnetic-ring positive stiffness mechanism and disc spring negative stiffness mechanism in parallel without a supporting surface. Further, the vertically downward direction was defined as positive when the mass of the isolated object was denoted as *m*. Consequently, when the loading platform moved downward, the recovery force, $f(x)$, of the vibration isolator was simultaneously provided by the magnetic rings and disc springs. Thus, $f(x)$ of the system was expressed as follows:

$$\begin{aligned} f(x) &= F_c + F_d \\ &= 2.362\times10^{-4}x^3 - 2.054\times10^{-5}x^2 + 0.326\,9x + 0.115\,9 + \\ &\left(\frac{4E}{1-\mu^2}\right)\left(\frac{t^4}{K_1D^2}\right)\left(\frac{x}{t}\right)\left[\left(\frac{h_0}{t}-\frac{x}{t}\right)\left(\frac{h_0}{t}-\frac{x}{2t}\right)+1\right] \end{aligned} \tag{7}$$

Further, the expression for the stiffness calculation can be obtained by differentiating Equation (7):

$$\begin{aligned} K(x) &= 7.086\times10^{-4}x^2 - 4.108\times10^{-5}x + 0.326\,9 + \\ &K_4^2\left(\frac{4E}{1-\mu^2}\right)\left(\frac{t'^3}{K_1D^2}\right)\left[K_4^2\left(\left(\frac{h_0'}{t'}\right)^2 - 3\left(\frac{h_0'}{t'}\right)\left(\frac{x}{t'}\right) + \frac{3}{2}\left(\frac{x}{t'}\right)^2\right) + 1\right] \end{aligned} \tag{8}$$

Figures 16 and 17 show the trends of the output force and stiffness of the magnetic positive-stiffness mechanism, respectively, as a function of axial displacement. When the disc spring compression exceeded 5.6 mm, the force generated by the springs correlated negatively with the compression of the disc spring, exhibiting a negative-stiffness characteristic. This behavior persisted until the compression reached 15 mm. Furthermore, when combined in parallel with the disc spring negative-stiffness mechanism, the load-bearing capacity of the system increased significantly. Moreover, the stiffness within the axial displacement range of 6.5–14 mm was notably lower, and no negative stiffness was observed within this specific interval. If the equilibrium position of the system was located within this low-

stiffness region, the system would exhibit unique structural characteristics: high and low static and dynamic stiffness, respectively, thereby achieving superior vibration isolation performance.

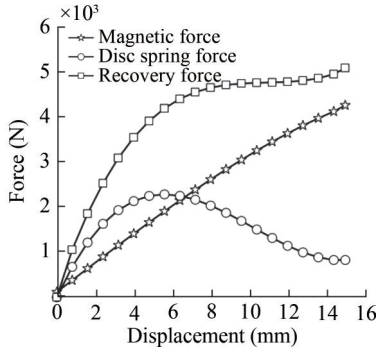


Figure 16 Comparison of the recovery force ($f(x)$)–displacement curves

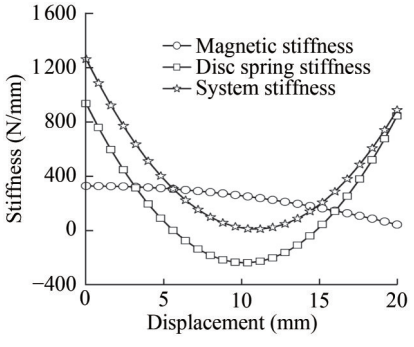


Figure 17 Comparison of $f(x)$–displacement curves

Assuming that the proposed magnetic-ring QZS vibration isolator deforms only in the vertical direction (x) under mass, Equations (7)–(8) can be approximated and fitted using a third-order polynomial to enable subsequent dynamic characterizations.

$$F_t = a_1 x^3 + a_2 x^2 + a_3 x + a_4 \tag{9}$$

where a_1 = 3.714, a_2 = −119.69, a_3 = 1294.28, a_4 = 46.87, and F_t is the fitting recovery force.

As shown in Figure 18, the F_t curve correlated well with the theoretical $f(x)$ curve, making it suitable for subsequent dynamic characterizations.

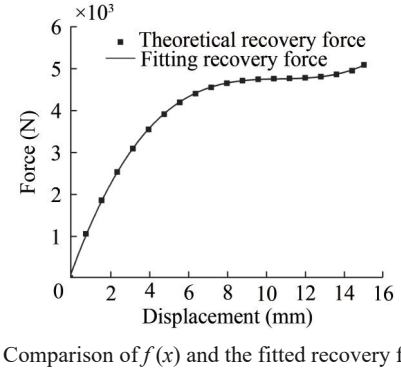


Figure 18 Comparison of $f(x)$ and the fitted recovery force (F_t)

3.2 Analysis of the amplitude–frequency characteristics

Assuming that the isolated object exhibited a mass of m and that the system damping ratio was c, the system (the magnetic-ring QZS vibration isolator assembly plus the isolated object) would reach static equilibrium when the object is loaded onto the vibration isolator. At this point, the displacement would be denoted as x_0, where the gravitational force of the system would be exactly counterbalanced by $f(x)$, indicating the zero-stiffness point.

$$mg = 3.714x_0^3 - 119.69x_0^2 + 1\,294.28x_0 + 46.87 \tag{10}$$

By combining the magnetic-ring positive stiffness mechanism and the disc spring negative-stiffness mechanism in parallel, the QZS vibration isolator was constructed. The total system stiffness was denoted as k_s. When the harmonic force, $F_0\cos(\omega t)$, was applied vertically downward to the isolated object, the object with mass m underwent a displacement, x_0, in the vertical direction. The dynamic model of the vibration isolator is illustrated in Figure 19.

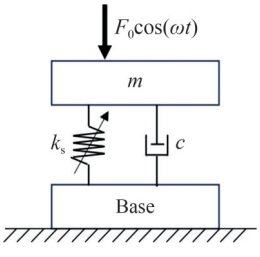


Figure 19 Structural schematic diagram of the vibration isolator

Based on Newton's second law, the nonlinear differential equation governing the motion of the system was derived, as follows:

$$m\ddot{x} = mg - c\dot{x} - F \tag{11}$$

Equation (11) was transformed into a differential equation describing the dynamic motion of the system under harmonic excitation:

$$m\ddot{x} + c\dot{x} + F = mg + F_0\cos(\omega t) \tag{12}$$

where $F = a_1(x + x_0)^3 + a_2(x + x_0)^2 + a_3(x + x_0) + a_4$.

Furthermore, a simplification of Equation (12) yields (13):

$$m\ddot{x} + c\dot{x} + \left(3a_1x_0^2 + 2a_2x_0 + a_3\right)x + \left(3a_1x_0 + a_2\right)x^2 + a_1x^3 = F_0\cos(\omega t) \tag{13}$$

Assuming that the steady-state response of the system

under harmonic excitation was expressed by the following:

$$x(t) = A\sin\left(\omega t + \varphi\right) \tag{14}$$

The characteristic equation of the system under harmonic excitation can be obtained by substituting Equation (14) into (13), neglecting the higher-order harmonic terms and equating the harmonic coefficients on both sides (Li et al., 2021):

$$\begin{cases} -mA\omega^2 + \left(3a_1x_0^2 + 2a_2x_0 + a_3\right)A + \dfrac{3a_1A^3}{4} = F_0\sin\varphi \\ cA\omega = F_0\cos\varphi \end{cases} \tag{15}$$

The system amplitude–frequency response equation was obtained by Pythagoras' theorem:

$$\left(-mA\omega^2 + \left(3a_1x_0^2 + 2a_2x_0 + a_3\right)A + \frac{3a_1A^3}{4}\right)^2 + \left(cA\omega\right)^2 = F_0^2 \tag{16}$$

Assuming that the system was subjected to a load of m = 470 kg, the corresponding static equilibrium displacement, x_0, would be 10 mm. The external harmonic excitation exhibited an amplitude, F_0, of 10, and ζ of 0.2 (Sodano et al., 2005; Zhou et al., 2022; Zhu et al., 2022). The critical and system damping ratios were $c_c = 2\sqrt{mk_s} = 5976.62$ N·s/m. Figure 20 shows the amplitude – frequency response curve of the system.

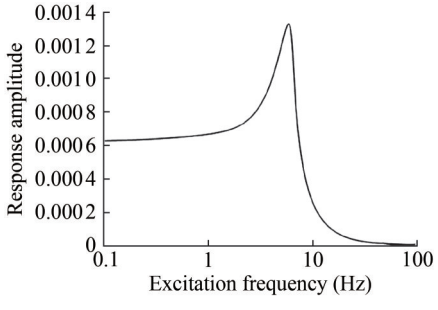


Figure 20 Curve of the amplitude–frequency characteristics of the system

3.3 Influence of the system parameters on force transmissibility

When the vibration isolator was subjected to a harmonic excitation force, $F_0\cos(\omega t)$, the transmitted force, f_t, on the base was considered the sum of the elastic and damping forces:

$$f_t = c \cdot x + F \tag{17}$$

Substituting $x = A\cos\left(\omega t + \varphi\right)$ into Equation (17) yields (18):

$$f_t = -c \cdot \omega \cdot x \cdot \sin\left(\omega t + \varphi\right) + F \tag{18}$$

Further, the amplitude, $|f_0|$, of the force transmitted to the base is expressed as follows:

$$|f_0| = \sqrt{(c\omega x)^2 + F^2} \tag{19}$$

T_e was defined as the ratio of $|f_0|$ to the amplitude of the external input force (F_0). To enable a more intuitive analysis of T_e variations across different vibration isolators, it was typically expressed in decibels to represent vibration isolation performance. Therefore, the decibel (dB) was adopted as the unit of T_e in this study.

$$T_e = 20 \cdot \lg\left(\frac{|f_0|}{F_0}\right) = 20 \cdot \lg\left(\frac{\sqrt{(c\omega x)^2 + F^2}}{F_0}\right) \tag{20}$$

Equation (20) reveals a relationship between F_0 and T_e at constant structural parameters of the vibration isolator. To investigate the influence of F_0 on T_e and elucidate the dynamic performance of the QZS vibration isolator, the effect of F_0 on the T_e characteristics of the system was investigated.

At stable system m and c, the influence of system parameter variations on the T_e characteristics of the vibration isolator was analyzed. To do this, the system parameters were set as follows: m = 470 kg and c = 1 195.32 N·s/m. Figure 21 illustrates the effect of F_0 on T_e. At F_0 of 1, 10, and 100 N, the corresponding natural frequencies were 0.84, 0.97, and 1.91 Hz, respectively, whereas the peak T_e values were 6.97, 8.19, and 12.2 dB, respectively. These results indicated that the natural frequency and T_e of the QZS vibration isolator increased with F_0 with respect to the natural frequency. Additionally, the downward jump frequency also increased, producing a higher initial isolation frequency and a reduced isolation bandwidth. This weakened the system's capability to isolate low-frequency vibrations. However, in the 20 – 100 Hz frequency range, T_e remained largely unaffected by F_0, as the increase in F_0 drove the system into the nonlinear region, resulting in an enlarged response amplitude and an increased $f(x)$, which consequently amplified the force transmitted to the base, as reflected by the increase in T_e.

Further, the system parameters were set as follows: m = 470 kg and F_0 = 10 N. Figure 22 illustrates the effect of F_0 on T_e of the vibration isolator under this condition. At c of 0.1, 0.2, and 0.4, the corresponding natural frequencies were 0.83, 0.97, and 1.16 Hz, respectively, whereas the corresponding peak T_e were 1.9, 8.19, and 15.1 dB, respectively. An increase in c resulted in the reduction of the resonance frequency and peak T_e in the low-frequency region,

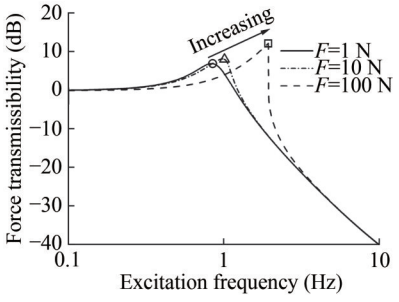


Figure 21 Effect of the excitation amplitude (F_0) on T_e

thereby enhancing the system's vibration isolation performance and weakening its nonlinear characteristics. When c exceeded a certain threshold, the jump phenomenon also disappeared. As the jump phenomena were among the typical features of nonlinear systems, the damping ratios reduced the sensitivity of the system to F_0 by suppressing the multivalued nature of nonlinear responses, thereby ensuring the stability of the system at a lower frequency and causing the jump phenomena to occur at this frequency. However, in the high-frequency region, T_e increased with c, causing a reduction in the system's vibration isolation performance. Under optimal conditions of the other parameters, appropriately increasing c lowered the downward jump frequency and initial isolation frequency. In engineering applications, c must be selected based on the actual operating frequency range when designing QZS vibration isolators to ensure optimal low-frequency vibration isolation performance.

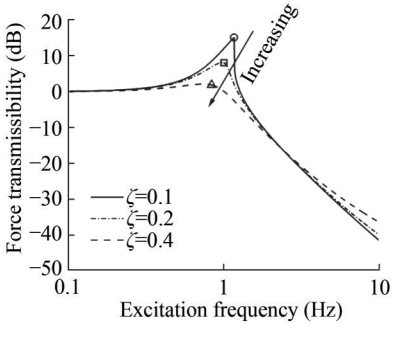


Figure 22 Effect of the damping ratio (c) on T_e

4 System validation through numerical simulation

To verify the accuracy of the implemented theoretical calculations, harmonic response analysis was performed using the commercial software, ANSYS. First, the dynamic simulation model of the vibration isolator was established. Thereafter, the mass of the load, m = 470 kg, was simulated on the loading platform, with stiffness and damping values that were consistent with those employed in previous reported theoretical analysis. Thereafter, the harmonic excitation with an amplitude of 10 N was applied to the loading platform, and the sweeping frequency range was set from 0 to 10 Hz, with an increment of 0.01 Hz. Finally, the reaction force at the base of the vibration isolator was extracted, followed by the computation of T_e using Equation (18). Notably, the disc spring negative-stiffness mechanism did not contribute to the system's behavior in the equivalent linear vibration-insulator system.

Figure 23 shows the comparison between the theoretical and simulated T_e of the vibration isolator, and Figure 24 shows the comparison between the T_e of the QZS vibration isolator and its equivalent linear system.

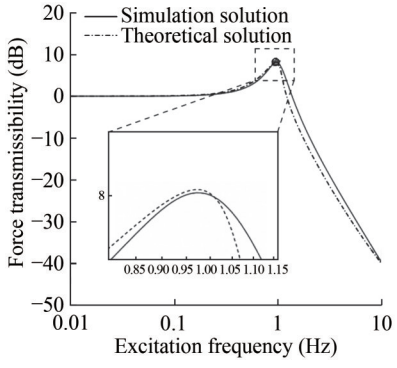


Figure 23 Comparison of theoretical and simulated T_e

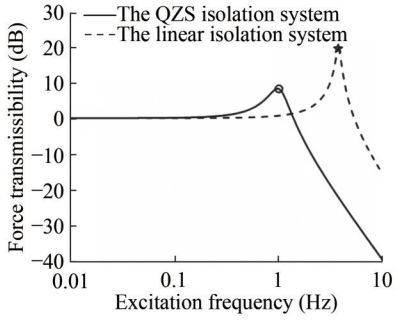


Figure 24 Comparison of the performances of the proposed QZS vibration isolator and its equivalent linear vibration isolator

As shown in Figure 23, the simulation and theoretical results correlated well. Both methods yielded an initial natural frequency of 0.97 Hz, with a peak T_e deviation of 1.14% at the natural frequency and a maximum error of 3.82 dB. These findings validate the reliability of the theoretical analysis. As depicted in Figure 24, at F_0 of 10 N and ζ of 0.2, the resonance frequency of the equivalent linear vibration isolator was 3.69 Hz, with a corresponding T_e peak of 19.25 dB. These results confirmed that the proposed QZS vibration isolator exhibited superior vibration isolation performance compared with its equivalent linear counterpart.

To further validate the low-frequency vibration isolation performance of the proposed QZS vibration isolator, an experimental study was conducted using a scaled-down

test platform based on a magnetic thrust bearing (Figure 25). First, the shaker was activated to apply random excitation to the test platform. Next, the amplitude of the reaction force at the base of the magnetic thrust bearing was extracted and utilized as the excitation source for the QZS vibration isolator and its equivalent linear system. The placement of force sensors at the reaction force measurement points is illustrated in Figure 26. Finally, numerical simulations were performed to compare the forces transmitted to the bases of both vibration isolation systems under identical excitation conditions. The effectiveness of the proposed QZS vibration isolator was verified by analyzing the comparative results.

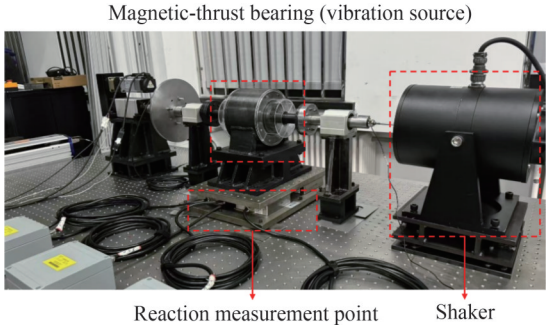


Figure 25 Experimental setup of magnetic-thrust bearing shrinkage test bench

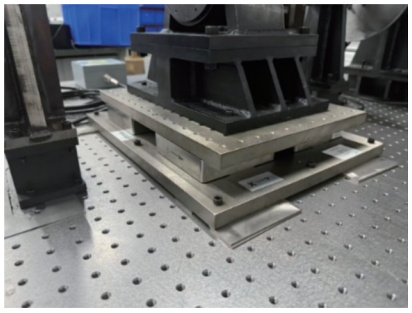


Figure 26 Arrangement of sensors at the reaction poin

Figure 27 shows the amplitude of the reaction force extracted from the base of the scaled-down magnetic bearing test platform. The time domain signal was sampled at an interval of 2 s, and the frequency domain signal covered a frequency range of 0–150 Hz.

As shown in Figure 28(a), the reaction force transmitted to the base through the QZS vibration isolator exhibited smaller fluctuations and lower vibration amplitude compared with that transmitted through its equivalent linear vibration isolator. Furthermore, Figure 28(b) shows that the QZS vibration isolator exhibited a broader isolation bandwidth and a lower initial isolation frequency compared with its equivalent linear system. Therefore, the QZS vibration isolator demonstrated in this study exhibited superior low-frequency vibration isolation performance compared with its equivalent linear system.

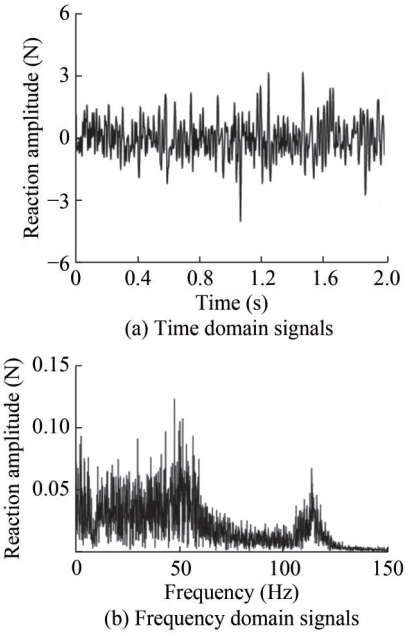


Figure 27 Stator reaction force signal measured on the magnetic thrust bearing test bench

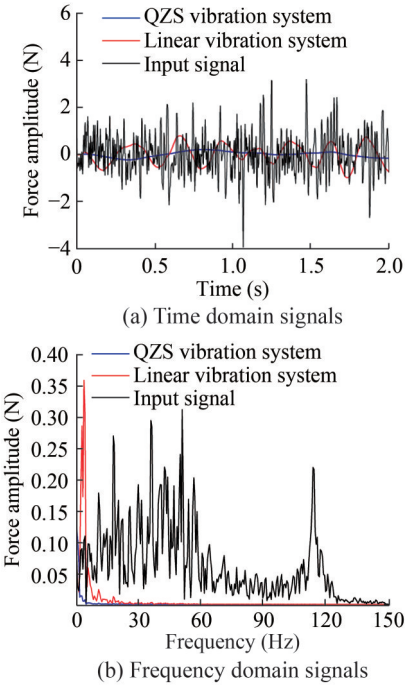


Figure 28 Comparison of the input and output force amplitudes

5 Conclusions

In this study, a low-frequency QZS vibration isolator was designed, and it effectively isolated low-frequency vibrations. By integrating theoretical analysis with simulations, the dynamic characteristics of the QZS vibration isolator were comprehensively investigated. The main conclusions of this study are summarized below.

1) A magnetic-ring QZS vibration isolator, adaptable to various load conditions, was designed, and a corresponding dynamic model was established to analyze the system's amplitude–frequency characteristics, T_e performance, and F_0 effect on T_e. The vibration isolation performance of the QZS system was also evaluated under varying load and damping conditions. The calculated first-order natural frequency of the QZS vibration isolator was 0.97 Hz, with a corresponding T_e peak of 8.19 dB and an initial isolation frequency of 1.2 Hz, demonstrating excellent low-frequency vibration isolation performance.

2) The accuracy of the isolation system design and theoretical analysis was verified through simulations. The deviation of the simulation from the theoretical calculations at the natural frequency was only 1.14%, with a maximum deviation of 3.82 dB in the 0–10 Hz frequency range.

3) A scaled-down magnetic bearing test platform was employed to obtain the reaction force at the base. This platform was subsequently utilized as an excitation source. Through simulation analysis, the amplitude of the signals of the transmitted force to the bases of the compared vibration isolators was determined. The final analysis of their vibration isolation performances revealed that the proposed magnetic ring QZS vibration isolator exhibited superior low-frequency vibration isolation capabilities.

Overall, the utilization of a Halbach magnet array was proposed for the positive-stiffness mechanism, offering advantages over linear springs in terms of torsion resistance and load offset resistance. Additionally, the magnetic ring QZS vibration isolator exhibited high load-bearing capacity, a low initial isolation frequency, and a broad isolation bandwidth, making it suitable for vibration isolator in naval electromechanical equipment and precision instruments. The primary limitation of this study is the lack of a fabricated prototype QZS vibration isolator and its subsequent experimental validation. Therefore, future studies will focus on bridging this gap by refining the theoretical framework and conducting comprehensive experimental investigations.

Competing interests The authors have no competing interests to declare that are relevant to the content of this article.

Reference

Cai CQ, Zhou JX, Wu LC, Wang K, Xu DL, Ouyang HJ (2020) Design and numerical validation of quasi-zero-stiffness metamaterials for very low-frequency band gaps. Composite Structures 236. https://doi.org/10.1016/j.compstruct.2020.111862

Chai K, Lou LJ, Yang QC, Liu SY (2017) Characteristic analysis of vibration isolation system based on high-static-low-dynamic stiffness. Journal of Vibroengineering 19(6): 4120-4137. https://doi.org/10.21595/jve.2017.18268

Dalela S, Balaji PS, Jena DP (2022) Design of a metastructure for vibration isolation with quasi-zero-stiffness characteristics using bistable curved beam. Nonlinear Dynamics 108(3): 1931-1971. https://doi.org/10.1007/s11071-022-07301-0

Davis RB, McDowell MD (2017) Combined Euler column vibration isolation and energy harvesting. Smart Materials and Structures 26(5). https://doi.org/10.1088/1361-665X/aa6721

Dong GX, Zhang XN, Luo YJ, Zhang YH, Xie SL (2018) Analytical study of the low frequency multi-direction isolator with high-static-low-dynamic stiffness struts and spatial pendulum. Mechanical Systems and Signal Processing 110: 521-539. https://doi.org/10.1016/j.ymssp.2018.03.041

Hao RB, Lu ZQ, Ding H, Chen LQ (2022) A nonlinear vibration isolator supported on a flexible plate: analysis and experiment. Nonlinear Dynamics 108(2): 941-958. https://doi.org/10.1007/s11071-022-07243-7

Li YY, Zhou XB, Chen WD, Liu XT (2021) Dynamic characteristics and application restrictions of a two-stage vibration isolation system with high-static-low-dynamic stiffness. Journal of Vibration Engineering 34(2). https://doi.org/10.16385/j.cnki. issn.1004-4523.2021.02.017

Liu CR, Yu KP, Liao BP, Hu RP (2021) Enhanced vibration isolation performance of quasi-zero-stiffness isolator by introducing tunable nonlinear inerter. Communications in Nonlinear Science and Numerical Simulation 95. https://doi.org/10.1016/j.cnsns.2020.105654

Liu CR, Zhao R, Yu KP, Lee HP, Liao BP (2021) A quasi-zero-stiffness device capable of vibration isolation and energy harvesting using piezoelectric buckled beams. Energy 233. https://doi.org/10.1016/j.energy.2021.121146

Liu Y, Sun FF, Yang JQ, Zeng C (2024) Development and experimental study of disc spring-based negative-positive-uncoupled stiffness devices for structural multi-level seismic fortification. Journal of Building Engineering 95. https://doi.org/10.1016/j.jobe.2024.110231

Lu DC, Zhou Y, Ma KQ, Lu L (2024) Investigation on the free vibration characteristics of vertical quasi-zero stiffness isolation system considering the disc spring's loading position. Soil Dynamics and Earthquake Engineering 178. https://doi.org/10.1016/j.soildyn.2024.108484

Ma KQ, Zhou Y, Lu DC (2023) Theoretical and experimental investigation on disc spring isolation system with loading rings. Soil Dynamics and Earthquake Engineering 165. https://doi.org/10.1016/j.soildyn.2022.107655

Ozaki S, K Tsuda, Tominaga J (2012) Analyses of static and dynamic behavior of coned disk springs: Effects of friction boundaries. Thin-Walled Structures 59: 132-143. https://doi.org/10.1016/j.tws.2012.06.001

Sodano Henry A, Bae Jae-Sung, Inman Daniel J, Keith Belvin W (2005) Concept and model of eddy current damper for vibration suppression of a beam. Journal of Sound and Vibration, 288(4-5): 1177-1196 .https://doi.org/10.1016/j.jsv.2005.01.016

Tian LL, Wu SH, Tian YQ (2017) Structure Optimization of Halbach Permanent Magnetic Bearing Constituted by Rectangular Section Permanent Magnetic Rings. Power System and Clean Energy 33(11). https://doi.org/CNKI:SUN:SXFD.0.2017-11-012

Tian YS, Cao DQ, Chen C, Zhang XY (2023) Vibration isolation performance of a rectangular panel with high-static-low-dynamic stiffness supports. Applied Mathematical Modelling 119: 218-238. https://doi.org/10.1016/j.apm.2023.02.027

Wang MT, Su P, Liu SY, Chai K, Wang BX, Lu JF (2022) Design and Analysis of Electromagnetic Quasi-zero Stiffness Vibration Isolator. Journal of Vibration Engineering & Technologies 11(1): 153-164. https://doi.org/10.1007/s42417-022-00569-x

Yan B, Ma HY, Zhao CX, Wu CY, Wang K, Wang PF (2018) A vari-

stiffness nonlinear isolator with magnetic effects: Theoretical modeling and experimental verification. International Journal of Mechanical Sciences 148: 745-755. https://doi.org/10.1016/j.ijmecsci.2018.09.031

Zhang Y, Liu QH, Lei YG, Cao JY, Liao WH (2023) Halbach high negative stiffness isolator: Modeling and experiments. Mechanical Systems and Signal Processing 188. https://doi.org/10.1016/j.ymssp.2022.110014

Zhang YS, Hou F, Lu ZQ, Ding H, Chen LQ (2025) Analytical and experimental study of thermoplastic polyurethane inclined beam isolator with quasi-zero stiffness and fractional derivative damping. Mechanical Systems and Signal Processing 224. https://doi. org/10.1016/j.ymssp.2024.111962

Zhou JX, Wang XL, Xu DL, Bishop S (2015) Nonlinear dynamic characteristics of a quasi-zero stiffness vibration isolator with cam–roller–spring mechanisms. Journal of Sound and Vibration 346: 53-69. https://doi.org/10.1016/j.jsv.2015.02.005

Zhou ZH, Dai ZH, Liu ZQ, Liu X, Chen SH, Li ZH, Zhou MR (2022) An adjustable low frequency vibration isolation with high-static-stiffness low-dynamic-stiffness property using a novel negative stiffness element. Applied Acoustics 188. https://doi.org/10.1016/j.apacoust.2021.108571

Zhu L, Zhou T, Wu YW, Bai HB, Tang Y (2022) Modeling and Performance Analysis ofVibration Isolation Systems with Parallel Connection of Positive and Negative Stiffness. Noise and Vibration Control. https://doi.org/10.3969/j.issn.1006-1355.2022.05.044